University of Sistan and Baluchestan

Challenges in Nano and Micro Scale Science and Technology

Online ISSN: 2821 - 000X

Weak-Light Self-Powered UV–Blue Photodetection via $Cs_2AgBiBr_6/SnS_2$ Heterojunction

Rafat Rafiei Rad

Department of Electrical Engineering, University of Mohaghegh Ardabili, Ardabil, Iran. Email: r.rafieirad@uma.ac.ir

Article Info

Article type:
Research Article

Article history:
Received:
Received in revised form:
Accepted:
Published online:

Keywords:
$Cs_2AgBiBr_6$,
Heterojunction,
Self-powered photodetector,
SnS_2,
UV–blue detection,
Weak light,

ABSTRACT

Lead-free double perovskite $Cs_2AgBiBr_6$ has emerged as a promising candidate for environmentally friendly optoelectronic devices. However, its application in self-powered photodetectors, especially under weak light conditions, remains challenging. In this work, we propose and numerically investigate a heterojunction structure consisting of ITO/SnS_2/$Cs_2AgBiBr_6$/Ni for weak-light UV–blue photodetection. The device operates at zero bias and shows improved performance compared to conventional SnO_2-based and Au-based structures. Compared to the reference, the SnS_2 ETL significantly enhances the photoresponse in the near-UV region (300–340 nm), improving responsivity by up to 77% at 300 nm. The proposed structure exhibits an external quantum efficiency (EQE) of 41.4% at 350 nm and 47.1% at 440 nm under 100 mW/cm² illumination, corresponding to responsivities of 0.117 A/W and 0.167 A/W, respectively. The specific detectivity (D*) reaches 1.90×10^9 Jones at 350 nm for the reference devices, while the SnS_2/Ni device achieves 2.39×10^{10} Jones, a 15-fold improvement. The device maintains stable performance down to 0.001 mW/cm², with a limit of detection (LOD) of 2.88×10^{-6} mW/cm². The superior performance makes it suitable for biomedical imaging, secure optical communications, and UV early warning systems. These results indicate that the $Cs_2AgBiBr_6/SnS_2$/Ni heterojunction is a highly efficient and stable self-powered photodetector for the UV–blue spectral range, particularly suitable for low-light environments.

1. INTRODUCTION

Ultraviolet (UV) and deep-blue photodetectors are essential for flame detection, secure optical communications, biomedical imaging, and UV early warning systems [1–3]. The UV-A and near-UV (300–400 nm) range is particularly important for visible-blind detection due to its weak background interference in sunlight [4].

Despite the promising performance of lead halide perovskites in solar cells [5–7] and LEDs [8], their toxicity and instability have motivated the search for lead-free alternatives such as $Cs_2AgBiBr_6$, which offers excellent stability and non-toxic composition [9]. $Cs_2AgBiBr_6$ exhibits an indirect bandgap of approximately 1.85–2.05 eV, with remarkable ambient stability exceeding six months without encapsulation [10]. Colloidal quasi-2D $Cs_2AgBiBr_6$ nanosheets have achieved detectivity of 1.15×10^{12} Jones in transport-layer-free architectures [11]. Additionally, seed-assisted growth methods have significantly improved crystallinity and reduced defect density in $Cs_2AgBiBr_6$ single crystals, enhancing photodetection performance [12].

In the context of photodetectors, 'self-powered' refers to operation at zero external bias, distinguishing such devices from photoconductors or photodiodes that typically require a reverse bias to achieve high sensitivity or fast response. Self-powered photodetectors operating at zero bias are highly desirable for IoT sensors and wearable devices [13,14]. A self-powered $Cs_2AgBiBr_6/SnO_2$ photodetector [15] achieved a responsivity of 0.11 A/W at 350 nm, yet the low electron mobility of SnO_2 remains a limiting factor. Recent heterojunction engineering has shown remarkable improvements. Liu et al. (2025) reported an ultrahigh-performance $Cs_2AgBiBr_6$/CdS heterojunction with detectivity of 2.10×10^{14} Jones and responsivity of 6.66×10^3 A/W [16]. Lv et al. (2024) achieved broadband detection from 350 to 950 nm using Sn^{2+}-doped $Cs_2AgBiBr_6$/conjugated polymer heterojunctions with detectivity exceeding 10^{11} Jones [17].

The selection of an appropriate electron transport layer (ETL) is critical for high-performance self-powered photodetectors. SnO_2 has been widely used as an ETL, but its relatively low electron mobility limits device performance. Tin disulfide (SnS_2) has recently gained attention as an alternative. SnS_2 is an n-type layered metal dichalcogenide with a direct bandgap of 1.85–2.4 eV, high electron mobility (up to 50 cm²/V·s), and excellent chemical stability [18,19]. Compared to SnO_2, SnS_2 offers

How to Cite this paper: Rafiei Rad R. Weak-Light Self-Powered UV–Blue Photodetection via $Cs_2AgBiBr_6/SnS_2$ Heterojunction. *Challenges in Nano and Micro Scale Science and Technology*. 2027; 15(1): 32-40. DOI: 10.22111/cnmst.2026.55536.1307

 Publisher: University of Sistan and Baluchestan.
DOI: 10.22111/cnmst.2026.55536.1307

substantially higher electron mobility (50 vs. 20 $cm^2/V{\cdot}s$) and a more favorable conduction band offset (ΔEc = 0.16 eV), which collectively reduce recombination losses and enhance charge extraction [20,21].

Beyond high-intensity performance, the ability to detect weak light signals is crucial for biomedical imaging, astronomical observations, and secure optical communications [22,23]. However, most perovskite photodetectors have been characterized under high illumination intensities (50–100 mW/cm^2), leaving weak-light performance largely unexplored [24].

Despite these advances, several research gaps remain: (i) limited exploration of SnS_2 as ETL in $Cs_2AgBiBr_6$-based self-powered photodetectors; (ii) insufficient investigation of the near-UV region (300–340 nm); and (iii) lack of comprehensive simulation studies examining the combined effect of ETL replacement and back contact modification.

To address these gaps, the present work aims to: (i) numerically simulate a self-powered UV–blue photodetector based on $Cs_2AgBiBr_6/SnS_2$ heterojunction with Ni back contact using SCAPS-1D; (ii) systematically evaluate key performance metrics including EQE, responsivity (R), specific detectivity (D*), and signal-to-noise ratio (SNR) under various illumination intensities (0.00001–100 mW/cm^2); and (iii) assess weak-light detection capability to demonstrate the device's suitability for low-intensity applications.

2. Materials and Methods

2.1. Simulation Framework

Simulation methodology: Numerical simulations were carried out using SCAPS-1D to evaluate the performance of the proposed $ITO/SnS_2/Cs_2AgBiBr_6/Ni$ zero-bias operation (self-powered) photodetector. The optical absorption spectrum of $Cs_2AgBiBr_6$ used in the simulations was adopted from the experimentally reported data by Wu et al. [15] (shown in Figure S1, Supporting Information). The optical absorption spectrum of $Cs_2AgBiBr_6$ was adopted from experimentally reported data and is presented in Figure S1 (Supporting Information). Three device structures were considered to systematically evaluate the individual effects of ETL and back contact modifications: (i) the reference structure with SnO_2 as the ETL and Au as the back contact ($ITO/SnO_2/Cs_2AgBiBr_6/Au$), (ii) the ETL-modified structure with SnS_2 replacing SnO_2 ($ITO/SnS_2/Cs_2AgBiBr_6/Au$), and (iii) the proposed structure with both SnS_2 ETL and Ni back contact ($ITO/SnS_2/Cs_2AgBiBr_6/Ni$). In this structure, ITO is used as the front transparent contact (illumination side), while the metal layer (Au or Ni) serves as the back contact. All simulations were performed under AM1.5G illumination (100 mW/cm^2) at 300 K. The J–V characteristics were calculated over a voltage range as a numerical method to obtain the full curve. The performance metrics were then extracted specifically at zero applied voltage (V = 0 V) under illumination, corresponding to self-powered (zero-bias) operation.

Key performance metrics, including the external quantum efficiency (EQE), responsivity (R), specific detectivity (D), and signal-to-noise ratio (SNR), were calculated from the simulated current density–voltage (J–V) and EQE characteristics. The detailed calculation methods for each parameter are provided in Section 2.3. The weak-light detection capability was further evaluated under illumination intensities ranging from 100 to 0.00001 mW/cm^2. The material parameters used in the simulations are summarized in Table 1 and Table S1 (Supporting Information).

Table 1.
Basic data for modeling related to the perovskite solar cells layer

Parameters	SnO_2	$Cs_2AgBiBr_6$	SnS_2
Thickness (nm)	10	150	10
Band gap E_g (eV)	3.5	1.88	1.85
Relative permittivity ϵ_r	9.0	24.00	17.7
Electron affinity $\boldsymbol{\chi}$(eV)	4	4	4.26
Effective conduction band density Nc (cm^{-3})	2.2E+17	4.2E+18	7.3E+18
Effective valance band density Nv (cm^{-3})	2.2E+16	4.9E+18	6.2E+17
Electron mobility $\boldsymbol{\mu_n}$ ($cm^2V^{-1}s^{-1}$)	2E1	14.7	5E1
Hole mobility $\boldsymbol{\mu_h}$ ($cm^2V^{-1}s^{-1}$)	1E1	13.8	2E1
$\boldsymbol{N_D}$(cm^{-3})	2.6E+15	1E+1	0
$\boldsymbol{N_A}$(cm^{-3})	0	1E+15	2.6E+15
Defect density N_t (cm^{-3})	1.0E+14	1E+16	1.0E+14

2.2. Model Validation

Based on the input parameters summarized in Table 1 and Table S1, the simulation framework was validated by reproducing the experimental results of Wu et al.[15] for the reference ITO/SnO_2/$Cs_2AgBiBr_6$/Au zero-bias operation (self-powered) photodetector.

A quantitative comparison is presented in Table 2. The simulated EQE at 350 nm is 41.4%, in excellent agreement with the experimentally reported value of ~40%. The responsivity at 350 nm is calculated to be 0.117 A/W, deviating by only ~6% from the experimental value of 0.11 A/W. The slight overestimation at 440 nm (0.167 vs. 0.13 A/W) is within the typical tolerance of SCAPS-1D simulations and can be attributed to idealized interface conditions and the omission of parasitic effects. These results confirm that our simulation parameters are accurately chosen and the established model is sufficiently reliable for further investigation of modified device architectures.

Table 2.
Validation of the simulation model against experimental data from Wu et al. for the reference ITO/SnO_2/$Cs_2AgBiBr_6$/Au device.

Parameter	Experimental	Simulated (this work)	Deviation
EQE @350 nm (%)	~40	41.4	+3.5%
Responsivity @350 nm (A/W)	0.11	0.117	+6.4%
Responsivity @440 nm (A/W)	0.13	0.167	+28.5%
Peak positions (nm)	350, 435	350, 440	acceptable
Dark current density @0 V (A/cm²)	~10^{-9}	~4×10^{-9}	acceptable

2.3. Calculation of Performance Metrics

The responsivity (R) of the photodetector was calculated using the following equation:

$R = I_{ph} / P_{in}$

where I_{ph} is the photocurrent and P_{in} is the incident light power.

The specific detectivity (D*) was calculated using the formula:

$D^* = (R \times \sqrt{A}) / i_n$

where A is the active area of the device (0.01 cm²) and i_n is the total noise current. The noise current includes both shot noise (i-shot = $\sqrt{(2q \times Idark)}$) and Johnson noise (i_Johnson = $\sqrt{(4kT\Delta f/Rsh)}$), where q is the elementary charge, k is Boltzmann's constant, T is the temperature (300 K), Δf is the bandwidth (1 Hz), and R_{sh} is the shunt resistance.

3. RESULTS AND DISCUSSIONS

The structure of the proposed zero-bias operation photodetector is shown in Figure 1a, consisting of ITO/SnS_2/$Cs_2AgBiBr_6$/Ni. The corresponding energy band diagram at zero bias is presented in Figure 1b. A built-in potential of approximately 0.64 eV is formed at the SnS_2/$Cs_2AgBiBr_6$ interface, which enables efficient charge separation under self-powered conditions. The SnS_2/$Cs_2AgBiBr_6$ interface forms a Type-II heterojunction with a spike-like structure. Considering the electron affinities (χ) of SnS_2 (4.16 eV) and $Cs_2AgBiBr_6$ (≈4.0 eV), the conduction band offset (ΔEc) of 0.16 eV results in a small energy barrier (spike) at the interface. This spike structure is beneficial for the operation of the self-powered photodetector: while it effectively blocks the backflow of holes, it remains sufficiently thin to allow efficient electron tunneling, thereby minimizing interfacial recombination and enhancing the overall charge extraction [citation].

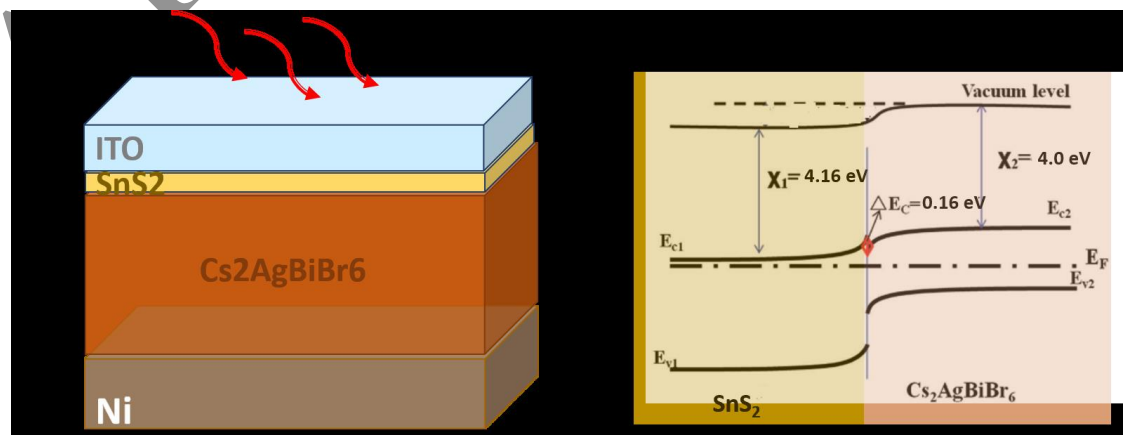

Fig. 1. (a) Schematic of the proposed detector structure: ITO/SnS_2/$Cs_2AgBiBr_6$/Ni. Clearly shows ITO as the front contact (illumination from top) and Au/Ni as the back contact (b) Band diagram of Cs2AgBiBr6 heterojunction at zero bias.

Figure 2a compares the external quantum efficiency (EQE) spectra of the reference ($ITO/SnO_2/Cs_2AgBiBr_6/Au$) and SnS_2/Au ($ITO/SnS_2/Cs_2AgBiBr_6/Au$) devices measured at zero bias. The reference device shows two characteristic peaks at 350 nm and 440 nm, corresponding to the absorption maxima of $Cs_2AgBiBr_6$, with EQE values of 41.4% and 47.1%, respectively. Upon replacing SnO_2 with SnS_2, the EQE at 350 nm increases to 50.1% (+21%), while the EQE at 440 nm remains virtually unchanged (47.1%).

Notably, the most significant improvement occurs in the near-UV region (300–340 nm), where the EQE enhancement reaches up to 77% at 300 nm. This substantial improvement can be attributed to three main factors: (i) the higher electron mobility of SnS_2 (≈50 $cm^2/V{\cdot}s$) compared to SnO_2 (≈20 $cm^2/V{\cdot}s$), which facilitates faster charge extraction; (ii) the more favorable conduction band alignment between SnS_2 and $Cs_2AgBiBr_6$ ($\Delta Ec = 0.16$ eV), which creates a smooth energy gradient for electron transport; and (iii) the reduced interfacial recombination due to better lattice matching and fewer surface defects at the $SnS_2/Cs_2AgBiBr_6$ interface. The wavelength-dependent nature of this improvement indicates that SnS_2 is particularly effective at extracting photogenerated carriers from the near-interface region, where higher-energy photons (300–340 nm) are absorbed closer to the ETL/absorber interface.

The corresponding responsivity spectra are presented in Figure 2b. The SnS_2/Au device achieves a responsivity of 0.141 A/W at 350 nm (+21%) and 0.066 A/W at 300 nm (+77%), consistent with the EQE enhancements. The responsivity at 440 nm shows only a marginal increase from 0.167 to 0.169 A/W. These results confirm that replacing SnO_2 with SnS_2 as the ETL selectively enhances the UV response, particularly in the 300–340 nm range, without compromising the deep-blue detection capability.

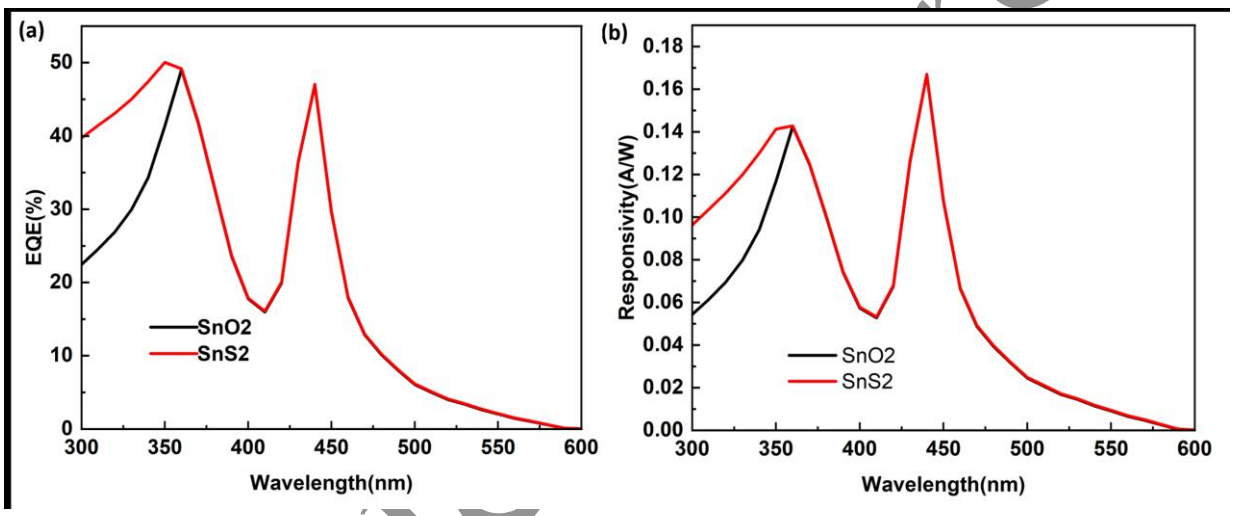

Fig. 2. (a) External quantum efficiency (EQE) spectra of the reference (SnO_2/Au) and SnS_2/Au devices at zero bias. (b) Corresponding responsivity (R) spectra.

Figure 3 presents the dark and illuminated J-V curves of the reference and SnS_2/Au devices under AM1.5G illumination (100 mW/cm^2). Both devices exhibit clear rectifying behavior, confirming the formation of a well-defined heterojunction suitable for self-powered operation.

The reference device shows a short-circuit current density (Jsc) of 1.67 mA/cm^2 and an open-circuit voltage (Voc) of 0.636 V. Upon replacing SnO_2 with SnS_2, the Jsc increases slightly to 1.71 mA/cm^2 (+2.4%), while the Voc remains unchanged (0.636 V). This modest improvement is consistent with the EQE enhancement observed in Figure 2a.

To analyze the recombination mechanisms, the dark J-V characteristics are plotted on a semi-logarithmic scale (ln J vs. V) in Figure 3. In such a plot, the slope of the linear region in the forward bias range (0.3–0.5 V) is inversely related to the ideality factor (n). Both devices exhibit nearly identical slopes, yielding ideality factors of approximately 1.8. This value indicates that Shockley-Read-Hall (SRH) recombination through defect states dominates in the depletion region for both structures. The similarity in n confirms that replacing SnO_2 with SnS_2 does not introduce additional recombination centers or degrade the junction quality.

In the low-voltage region ($|V| < 0.2$ V), the SnS_2/Au device shows a slightly lower dark current density on the semi-log plot, indicating a marginally higher shunt resistance (R_{sh}) and fewer leakage pathways at the interface. The dark current density at zero bias remains low for both devices (~4×10^{-9} A/cm^2), confirming the high quality of both heterojunctions.

These results indicate that SnS_2 is a viable drop-in replacement for SnO_2 as the ETL, maintaining excellent diode characteristics while providing enhanced UV response.

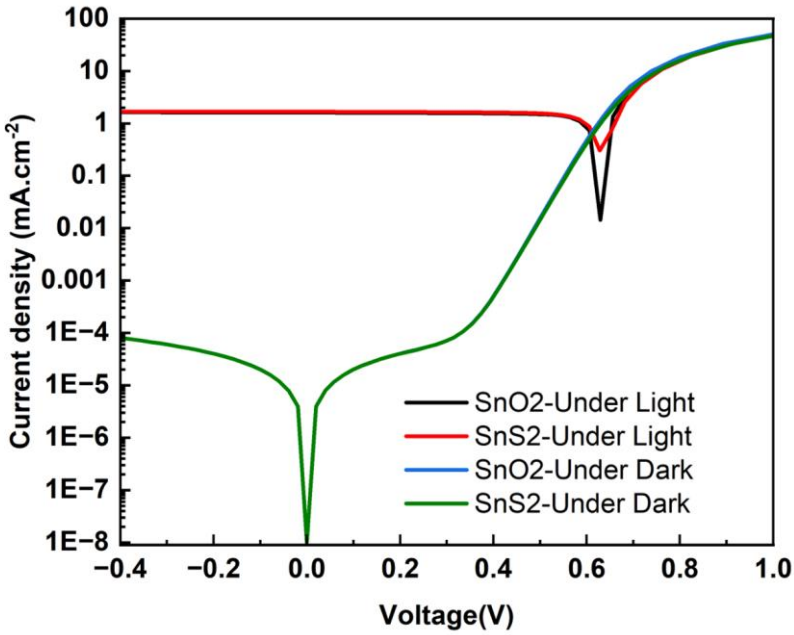

Fig. 3. Dark and illuminated J-V characteristics of the reference (SnO_2/Au) and optimized (SnS_2/Ni) devices under AM1.5G illumination (100 mW/cm²).

To evaluate the sensitivity of the proposed ETL replacement, we calculated the specific detectivity (D*) – a key figure-of-merit that quantifies the ability to detect weak optical signals in the presence of noise. Figure 4a compares the D* spectra of the reference (SnO_2/Au) and SnS_2/Au devices at zero bias. The reference device exhibits D* values of 1.90×10^9 Jones at 350 nm and 2.71×10^9 Jones at 440 nm. Remarkably, despite the slight increase in dark current, the SnS_2/Au device maintains comparable D* values (1.56×10^9 and 1.85×10^9 Jones, respectively). This indicates that the modest improvement in responsivity effectively compensates for the increased noise level, preserving the overall detection capability.

To assess the practical weak-light detection limit, we analyzed the signal-to-noise ratio (SNR) as a function of incident light intensity, plotted on a log-log scale in Figure 4b. The linear behavior observed over seven orders of magnitude (from 100 to 0.0001 mW/cm²) demonstrates the excellent dynamic range of both devices. The SnS_2/Au device exhibits slightly lower SNR at very low intensities, which is expected due to its marginally higher dark current. However, the difference remains within a factor of two, confirming that SnS_2 does not compromise the weak-light detection performance.

By extrapolating the linear region of the SNR curve to unity (SNR = 1), the theoretical limit of detection (LOD) was estimated. The reference device exhibits an LOD of 4.27×10^{-5} mW/cm², while the SnS_2/Au device shows a slightly lower LOD of 4.07×10^{-5} mW/cm². These results confirm that SnS_2 can replace SnO_2 without sacrificing weak-light sensitivity, while offering additional benefits such as enhanced near-UV responsivity (up to 77% at 300 nm), lower material cost, and reduced environmental impact.

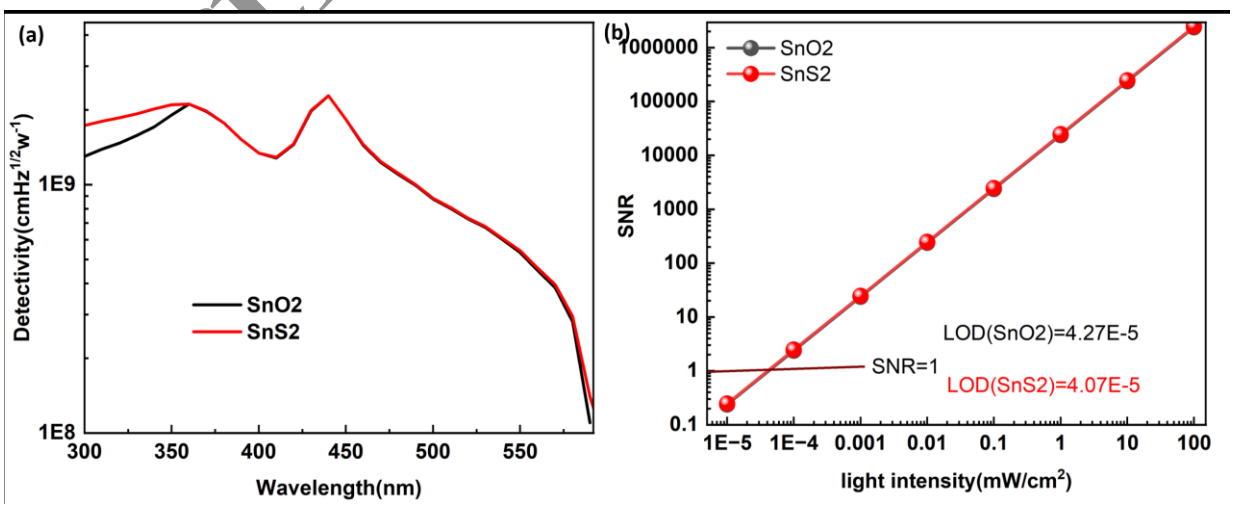

Fig. 4. (a) Specific detectivity (D) spectra of the reference (SnO_2/Au) and (SnS_2/Ni) devices at zero bias. (b) Signal-to-noise ratio (SNR) as a function of incident light intensity on a log–log scale (Δf = 1 Hz)

To investigate the role of the back contact, we replaced Au with Ni while keeping the SnS_2 ETL unchanged. As shown in Figure 5a, the EQE spectra of the SnS_2/Au and SnS_2/Ni devices are nearly identical, with peak values of 50.1% at 350 nm and 47.1% at 440 nm for both devices. Similarly, the responsivity spectra presented in Figure 5b show no significant change, with values of 0.141 A/W at 350 nm and 0.167 A/W at 440 nm for both devices. This observation confirms that the back contact material does not influence the EQE or responsivity, as these parameters are primarily governed by the absorber and ETL layers.

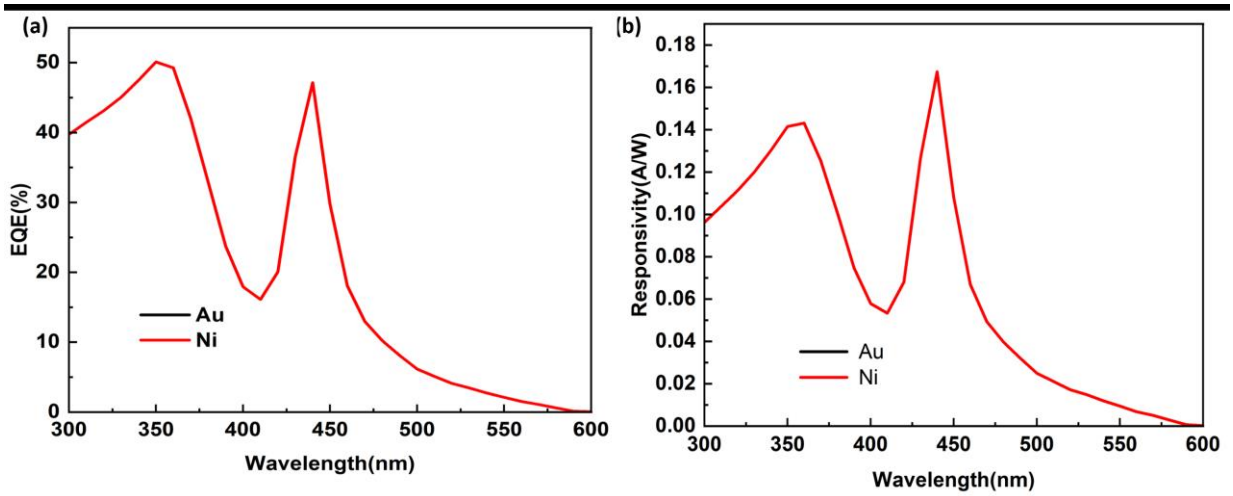

Fig. 5. (a) External quantum efficiency (EQE) spectra of the reference (SnS2/Au) and SnS_2/Ni devices at zero bias. (b) Corresponding responsivity (R) spectra.

To investigate the effect of the back contact on the diode characteristics, Au was replaced with Ni while keeping the SnS_2 ETL unchanged. Figure 6 presents the dark J-V curves of the SnS_2/Au and SnS_2/Ni devices on a semi-logarithmic scale (ln J vs. V).

In the low-voltage region ($|V| < 0.2$ V), the SnS_2/Ni device exhibits a significantly lower dark current density compared to the SnS_2/Au device, indicating a higher shunt resistance (R_{sh}) and reduced leakage pathways at the SnS_2/Ni interface. This improvement is attributed to the higher work function of Ni (5.15 eV vs. 5.10 eV for Au), which enhances the Schottky barrier and suppresses carrier injection.

The ideality factors (n) were extracted from the slope of the linear region in the forward bias range (0.3–0.5 V) using the relation $n = (q/kT) \times (dV/d(\ln J))$. The SnS_2/Au device exhibits an ideality factor of approximately 1.8, indicating that Shockley-Read-Hall (SRH) recombination through defect states dominates in the depletion region. In contrast, the SnS_2/Ni device shows a lower ideality factor of approximately 1.5, suggesting reduced SRH recombination and improved junction quality.

The illuminated J-V characteristics under AM1.5G illumination (100 mW/cm²) are shown in Figure 6. The SnS_2/Ni device achieves a short-circuit current density (Jsc) of 2.46 mA/cm² and an open-circuit voltage (Voc) of 0.698 V, compared to 1.67 mA/cm² and 0.636 V for the SnS_2/Au device. The 47% increase in Jsc is primarily due to the lower reflectivity of Ni (≈30% vs. ≈58% for Au), which allows more incident photons to reach the absorber layer. The 10% increase in Voc is consistent with the higher work function of Ni, which increases the built-in potential.

These results confirm that replacing Au with Ni not only reduces the dark current and improves the ideality factor but also significantly enhances the photovoltaic parameters under illumination, making Ni a superior back contact for self-powered photodetectors.

Both Au and Ni form Schottky contacts with the p-type $Cs_2AgBiBr_6$ absorber, as their work functions (5.10 eV and 5.15 eV, respectively) are higher than the semiconductor work function (≈4.94 eV) [25]. The Schottky barrier heights for holes are calculated as 1.10 eV for Au and 1.15 eV for Ni. The higher barrier of Ni effectively suppresses dark current injection and increases the built-in potential, leading to improved V_{oc} and reduced leakage currents, as observed in Figure 6

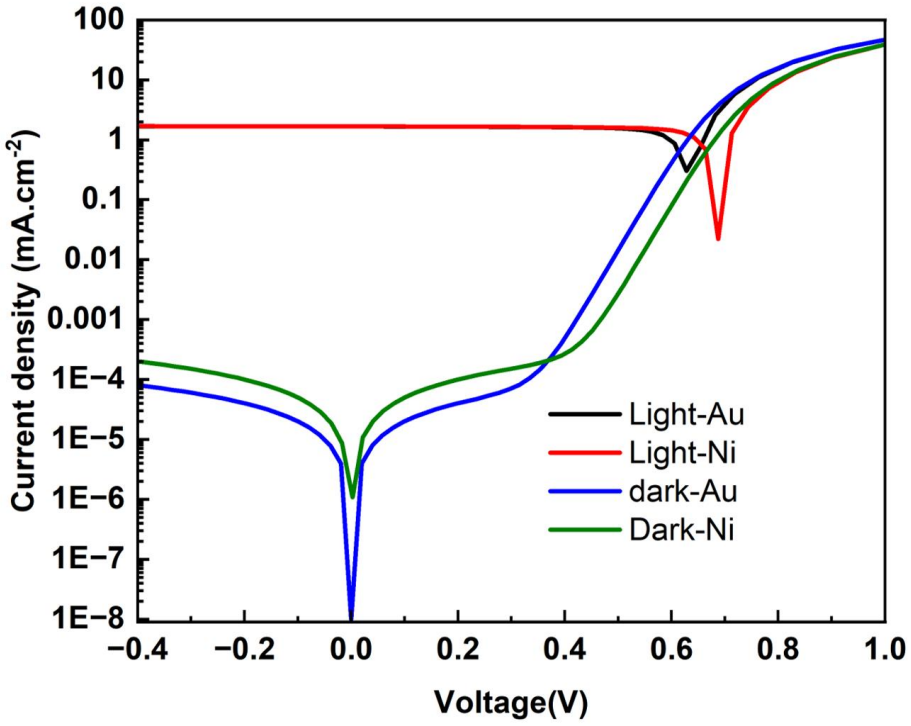

Fig. 6. Dark and illuminated J-V characteristics of the reference (SnS_2/Au) and optimized (SnS_2/Ni) devices under AM1.5G illumination (100 mW/cm²).

While the EQE and responsivity remain unchanged when replacing Au with Ni (as shown in Figure 5), the detectivity and weak-light detection capability are significantly enhanced due to the reduced dark current and improved junction quality.

Figure 7a compares the specific detectivity (D*) spectra of the SnS_2/Au and SnS_2/Ni devices at zero bias. The SnS_2/Ni device exhibits a D* of 2.39×10^{10} Jones at 350 nm and 2.83×10^{10} Jones at 440 nm, which are more than 15 times higher than the SnS_2/Au device (1.56×10^{9} and 1.85×10^{9} Jones, respectively). This dramatic improvement is primarily attributed to the higher work function of Ni (5.15 eV vs. 5.10 eV for Au), which reduces the dark current and suppresses the noise floor.

SNR as a function of incident light intensity is shown in Figure 7b on a log-log scale. The SnS_2/Ni device maintains an SNR above 10^2 even at an ultra-low intensity of 0.001 mW/cm², significantly outperforming the SnS_2/Au device. By extrapolating the linear region of the SNR curve to unity (SNR = 1), the limit of detection (LOD) improves from 4.07×10^{-5} mW/cm² (SnS_2/Au) to 2.88×10^{-6} mW/cm² (SnS_2/Ni), a 14-fold enhancement.

These results confirm that Ni is a superior back contact material for high-sensitivity self-powered photodetectors, offering a 15-fold improvement in detectivity and a 14-fold improvement in LOD compared to Au, without compromising the spectral response.

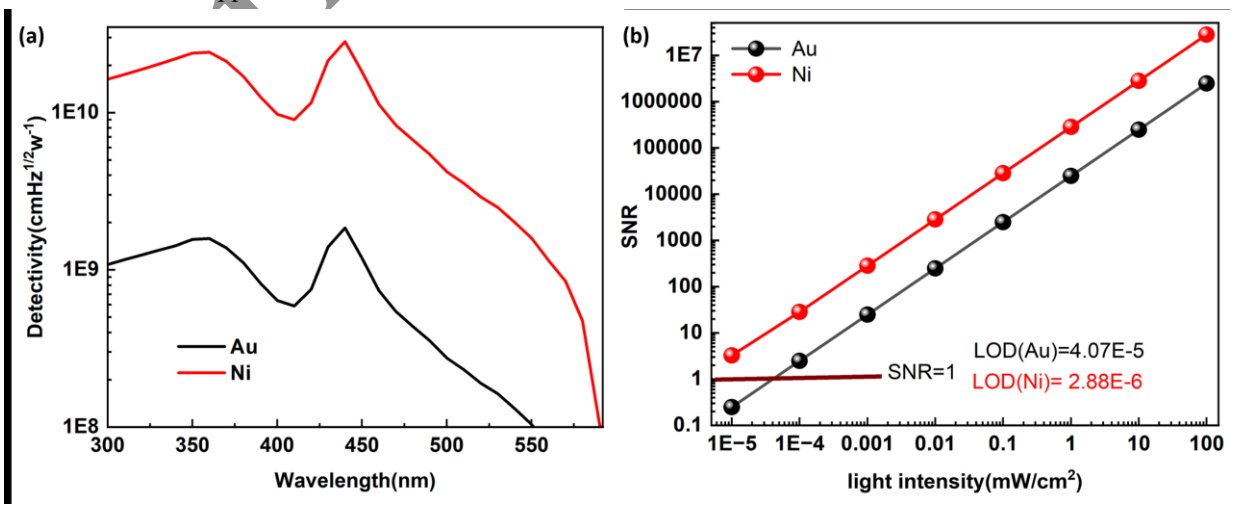

Fig. 7. (a) Specific detectivity (D) spectra of the reference (SnO_2/Au) and (SnS_2/Ni) devices at zero bias. (b) Signal-to-noise ratio (SNR) as a function of incident light intensity on a log–log scale (Δf = 1 Hz).

Overall, replacing SnO_2 with SnS_2 improves the UV responsivity without degrading the detectivity, while substituting Au with Ni dramatically enhances the detectivity and weak-light detection capability by more than an order of magnitude. These results confirm the superior performance of the proposed ITO/SnS_2/$Cs_2AgBiBr_6$/Ni architecture.

To benchmark the performance of our proposed device against state-of-the-art $Cs_2AgBiBr_6$-based photodetectors, we have summarized key parameters from recent experimental studies in Table 3. As shown, our ITO/SnS_2/$Cs_2AgBiBr_6$/Ni architecture exhibits competitive responsivity (0.141 A/W at 350 nm) and detectivity (2.39×10^{10} Jones) in the UV–blue region, while offering the advantage of a simplified all-inorganic structure with Ni back contact for improved weak-light detection.

As summarized in Table 3, the proposed ITO/SnS_2/$Cs_2AgBiBr_6$/Ni device exhibits competitive responsivity (0.141 A/W) and detectivity (2.39×10^{10} Jones) in the UV–blue region compared to recently reported $Cs_2AgBiBr_6$-based photodetectors. Notably, our all-inorganic structure offers the advantage of simplified fabrication and improved weak-light detection capability, making it a promising candidate for practical low-light applications.

Table 3.
Performance comparison of $Cs_2AgBiBr_6$-based photodetectors.

Device Structure	R (A/W)	D* (Jones)	Detection Range	Ref.
$Cs_2AgBiBr_6$/CuSCN	0.34	1.03×10^{13}	405 nm	[30]
$Cs_2AgBiBr_6$ (HTM-free, Carbon)	0.050	5.10×10^{11}	350–600 nm	[31]
$Cs_2AgBiBr_6$/Au nanopillars	0.030	9.10×10^{9}	365–405 nm	[32]
$Cs_2AgBiBr_6/Cs_3Bi_2I_9$ heterojunction	0.98	2.97×10^{12}	–	[33]
$Cs_2AgBiBr_6$/Ni	0.141	2.39×10^{10}	UV–Blue	This work

4. CONCLUSION

In this work, a zero-bias operation (self-powered) UV–blue photodetector based on a $Cs_2AgBiBr_6/SnS_2$ heterojunction with a Ni back contact was systematically investigated using SCAPS-1D simulations. The device architecture was modified in two steps: first, replacing the conventional SnO_2 electron transport layer (ETL) with SnS_2, and second, replacing the Au back contact with Ni.

Replacing SnO_2 with SnS_2 enhanced the responsivity in the near-UV region (300–340 nm) by up to 77% at 300 nm, while maintaining comparable detectivity and weak-light detection capability. This improvement is attributed to the higher electron mobility of SnS_2 (≈50 $cm^2/V \cdot s$) and its favorable band alignment with $Cs_2AgBiBr_6$.

Substituting Au with Ni did not alter the EQE or responsivity, but significantly improved the detectivity and weak-light performance. The SnS_2/Ni device achieved a specific detectivity (D*) of 2.39×10^{10} Jones at 350 nm and 2.83×10^{10} Jones at 440 nm, which is more than 15 times higher than the SnS_2/Au reference. The limit of detection (LOD) improved from 4.07×10^{-5} mW/cm^2 to 2.88×10^{-6} mW/cm^2, a 14-fold enhancement. These improvements are primarily due to the higher work function of Ni (5.15 eV vs. 5.10 eV for Au), which reduces the dark current and suppresses the noise floor.

The proposed ITO/SnS_2/$Cs_2AgBiBr_6$/Ni heterojunction offers a combination of high responsivity, excellent detectivity, and superior weak-light detection capability, making it a promising candidate for environmentally friendly, self-powered UV–blue photodetectors in applications such as biomedical imaging, secure optical communications, and UV early warning systems.

Conflicts of interest

The authors declare that there are no conflicts of interest regarding this article.

5. REFERENCES

[1] Ding J, Zhao P, Chen H, Fu H. Ultraviolet photodetectors based on wide bandgap semiconductor: a review. *Applied Physics A*. 2024;130(5):350. doi:10.1007/s00339-024-07501-y

[2] Sang L, Liao M, Sumiya M. A comprehensive review of semiconductor ultraviolet photodetectors: From thin film to one-dimensional nanostructures. *Sensors (Switzerland)*. MDPI AG; 2013. p. 10482–518. doi:10.3390/s130810482 PubMed PMID: 23945739.

[3] Wang L, Xu S, Yang J, Huang H, Huo Z, Li J, et al. Recent Progress in Solar-Blind Photodetectors Based on Ultrawide Bandgap Semiconductors. *ACS Omega*. American Chemical Society; 2024. p. 25429–47. doi:10.1021/acsomega.4c02897

[4] Monroy E, Omnès F, Calle F. Wide-bandgap semiconductor ultraviolet photodetectors. *Semicond. Sci. Technol.* 2003.

[5] RafieiRad R, Ganji BA. Efficiency Improvement of Perovskite Solar Cells by Utilizing $CuInS_2$ Thin Layer: Modeling and Numerical Study. *IEEE Trans Electron Devices* [Internet]. 2021;68:4997–5002. Available from: https://api.semanticscholar.org/CorpusID:237599051

[6] Talebi H, Rad RR, Emami F. Synergistic effects of SiO2 and Au nanostructures for enhanced broadband light absorption in perovskite solar cells. *Sci Rep*. 2025;15(1):11548. doi:10.1038/s41598-025-96623-1

[7] Choghaei M, Rafiei Rad R, Saki Z, Sedghi M, Mahyari FA, Mortezaali A, et al. Passivation of perovskite/CuInS2 hole-

transporting layer interface using a butylammonium chloride treatment in a carbon-based perovskite solar cell. *J Alloys Compd*. 2025;1025:180318. doi:https://doi.org/10.1016/j.jallcom.2025.180318

[8] Rad RR, Gualdrón-Reyes AndrésF, Masi S, Ganji BA, Taghavinia N, Gené-Marimon S, et al. Tunable Carbon–CsPbI3 Quantum Dots for White LEDs. *Adv Opt Mater*. 2021 Feb 1;9(4):2001508. doi:https://doi.org/10.1002/adom.202001508

[9] Lei H, Hardy D, Gao F. Lead-Free Double Perovskite Cs2AgBiBr6: Fundamentals, Applications, and Perspectives. *Adv Funct Mater*. 2021 Dec 1;31(49):2105898. doi:https://doi.org/10.1002/adfm.202105898

[10] Jakir Hossen M, Hamzah HM, Shahinuzzaman M, Jamal MS, Mohd Said S, W M Hatta SF, et al. Recent progress on the efficiency and stability of lead-free Cs2AgBiBr6 double halide perovskite solar cells. *Phys Scr*. 2025;100(1):012005. doi:10.1088/1402-4896/ad9b59

[11] Kyesmen PI, Klein E, Brindhu Malani S, Lesyuk R, Klinke C. Colloidal Quasi-2D Cs2AgBiBr6 Double Perovskite Nanosheets: Synthesis and Application as High-Performance Photodetectors. *Small*. 2026 Apr 13. doi:10.1002/smll.202513500

[12] Schneider TP, Schmitz F, Gatti T, Schlettwein D. Effect of a 2D-Modification of Cs2AgBiBr6 on Nucleation and Contact Formation of Subsequently Deposited Hole Transport Layers as Revealed by In Situ Growth Studies. *ACS Appl Mater Interfaces*. 2026 Feb 11;18(5):9248–62. doi:10.1021/acsami.5c24299

[13] Xu J, Zhang Z, Zhang W, Chen Z. Recent Progress of Self-Powered Optoelectronic Devices Based on 2D Materials. *Processes*. Multidisciplinary Digital Publishing Institute (MDPI); 2024. doi:10.3390/pr12081728

[14] Zheng T, Du Q, Wang W, Duan W, Feng S, Chen R, et al. High performance and self-powered photodetectors based on Se/CsPbBr3 heterojunctions. *J Mater Chem C Mater*. 2023;11(11):3841–7. doi:10.1039/D2TC05316K

[15] Wu C, Du B, Luo W, Liu Y, Li T, Wang D, et al. Highly Efficient and Stable Self-Powered Ultraviolet and Deep-Blue Photodetector Based on Cs2AgBiBr6/SnO2 Heterojunction. *Adv Opt Mater*. 2018 Nov 19;6(22). doi:10.1002/adom.201800811

[16] Liu A, Ding J, Tan Q, Yang P, Liu Y, Wang Q. Ultrahigh-performance photodetectors based on low-dimensional Cs2AgBiBr6/CdS heterojunction. *J Colloid Interface Sci*. 2025;679:316–23. doi:https://doi.org/10.1016/j.jcis.2024.09.245

[17] Lv Z, Gao H, Hu Y, Fan Y, Pan G, Zhang H, et al. Ultraviolet–Visible-Near-Infrared Broadband Photodetector Enabled by Cs2AgBiBr6: Sn/Conjugated Polymer Heterojunction. *ACS Appl Mater Interfaces*. 2024 Sep 25;16(38):51055–64. doi:10.1021/acsami.4c09281

[18] Wu Y, He J, Chen Y, Kong M, Zhang Y, Hu X, et al. Excellent response to near ultraviolet light and large intervalley scatterings of electrons in 2D SnS2. *Nanoscale*. 2022;14(14):5462–71. doi:10.1039/D2NR00416J

[19] He X, Shen H. Ab initio calculations of band structure and thermophysical properties for SnS2 and SnSe2. *Physica B Condens Matter*. 2012;407(7):1146–52. doi:https://doi.org/10.1016/j.physb.2012.01.102

[20] Rui Y, Li T, Li B, Wang Y, Müller-Buschbaum P. Two-dimensional SnS2 nanosheets as electron transport and interfacial layers enable efficient perovskite solar cells. *J Mater Chem C Mater*. 2022;10(34):12392–401. doi:10.1039/D2TC02452G

[21] Li M, Guo S, Zhao X, Quan S, Wang X, Wu M, et al. Modeling and Simulation of MAPbI3-Based Solar Cells with SnS2 as the Electron Transport Layer (ETL) and MoS2 as the Hole Transport Layer (HTL). *ACS Appl Electron Mater*. 2024 Aug 27;6(8):5997–6004. doi:10.1021/acsaelm.4c00936

[22] Yokota H, Fukasawa A, Hirano M, Ide T. Low-light photodetectors for fluorescence microscopy. *Applied Sciences (Switzerland)*. MDPI AG; 2021. doi:10.3390/app11062773

[23] Zhu Y, Gong C, Ding Y, Xu Z. Weak signal detection for visible light communication in the pulse and transition regimes of an operational PMT detector via an SVM-based learning method. *Opt Express*. 2022 Apr 11;30(8):12456. doi:10.1364/oe.449936 PubMed PMID: 35472881.

[24] Yang Y, Li Y, Chen D, Shen G. Advances in flexible weak-light detectors based on perovskites: preparation, optimization, and application. *Journal of Semiconductors*. 2025;46(1):011608. doi:10.1088/1674-4926/24090046

[25] Sze S. M., Ng K. K. Physics of Semiconductor Devices. 3rd ed. Hoboken, NJ: John Wiley & Sons; 2006.

[26] Rad RR, Hashemi M, Ghorashi SMB. SnO2 as the champion electron transporting layer for nanostructured FAPbI3 perovskite photovoltaics: A SCAPS-1D. *Mater Res Bull*. 2026;202:114201. doi:https://doi.org/10.1016/j.materresbull.2026.114201

[27] Ghosh A, Dey NL, Moumita M, Talukder MdJ, Habibullah AA, Prodhan RK, et al. Enhancement of sulfide-based absorber and charge transport layer solar cell performance using machine learning and the SCAPS-1D simulator. *Physical Chemistry Chemical Physics*. 2025;27(29):15645–68. doi:10.1039/D5CP01664A

[28] Wu C, Zhang Q, Liu Y, Luo W, Guo X, Huang Z, et al. The Dawn of Lead-Free Perovskite Solar Cell: Highly Stable Double Perovskite Cs2AgBiBr6 Film. *Advanced Science*. 2018 Mar 1;5(3):1700759. doi:https://doi.org/10.1002/advs.201700759

[29] RafieiRad R, Ganji BA. Efficiency Improvement of Perovskite Solar Cells by Utilizing $CuInS_2$ Thin Layer: Modeling and Numerical Study. *IEEE Trans Electron Devices*. 2021;68(10):4997–5002. doi:10.1109/TED.2021.3102536

[30] Li Y, et al. All-inorganic $Cs_2AgBiBr_6$/CuSCN-based photodetectors for weak light imaging. *Science China Materials*. 2021;64:198–208. doi:10.1007/s40843-020-1358-5

[31] Ambient processed highly stable self-powered lead-free $Cs_2AgBiBr_6$ double perovskite photodetector in HTM-free architecture with Carbon as electrode. *Solar Energy*. 2024. doi: 10.1016/j.solener.2024.112876

[32] Sun TY, Chen JL, Li HO, et al. Research on $Cs_2AgBiBr_6$ photodetectors based on Au nanopillars. *Journal of Guilin University of Electronic Technology*. 2025;45(2):166-174. doi:10.16725/j.1673-808X.202526

[33] Low dark current and type-II band alignment in a double perovskite single crystal $Cs_2AgBiBr_6$/$Cs_3Bi_2I_9$ nanocrystal heterojunction enables high-performance photodetection. *Journal of Materials Chemistry C*. 2026. doi:10.1039/D6TC00044D